



Seeding the Electrothermal Instability through a Three-Dimensional, Nonlinear Perturbation

E. P. Yu,^{1,*} T. J. Awe,¹ K. R. Cochrane,¹ K. J. Peterson,¹ K. C. Yates,^{1,2} T. M. Hutchinson^{1,3},, M. W. Hatch,⁴ B. S. Bauer,⁵ K. Tomlinson,⁶ and D. B. Sinars¹

¹Sandia National Laboratories, Albuquerque, New Mexico 87185, USA

²Los Alamos National Laboratory, Los Alamos, New Mexico 87545, USA

³Lawrence Livermore National Laboratory, Livermore, California 94550, USA

⁴University of New Mexico, Albuquerque, New Mexico 87131, USA

⁵University of Nevada, Reno, Reno, Nevada 89506, USA

⁶General Atomics, San Diego, California 92121, USA

 (Received 26 October 2021; revised 24 February 2023; accepted 17 May 2023; published 22 June 2023)

Electrothermal instability plays an important role in applications of current-driven metal, creating striations (which seed the magneto-Rayleigh-Taylor instability) and filaments (which provide a more rapid path to plasma formation). However, the initial formation of both structures is not well understood. Simulations show for the first time how a commonly occurring isolated defect transforms into the larger striation and filament, through a feedback loop connecting current and electrical conductivity. Simulations have been experimentally validated using defect-driven self-emission patterns.

DOI: [10.1103/PhysRevLett.130.255101](https://doi.org/10.1103/PhysRevLett.130.255101)

Introduction.—For decades, researchers have sought to harness the potential of metal driven by pulsed, intense electrical current, for applications including material property studies [1–5], radiation science [6,7], laboratory astrophysics [8,9], magnetic flux compression [10,11], and magnetoinertial fusion [12–21]. Experiments commonly drive electrical current density \mathbf{j} through cylindrical metallic shells (also known as liners), which then implode due to the interaction of the self-generated magnetic field \mathbf{B} with current (i.e., $\mathbf{j} \times \mathbf{B}$ force). Magnetically accelerated liners are susceptible to the magneto-Rayleigh-Taylor instability (MRTI) (e.g., Refs. [22–25]), which amplifies density perturbations on the outer surface of the liner. Assuming \mathbf{j} flows vertically, even initially smooth (~ 50 nm rms) liners develop horizontally oriented perturbations [26] that can degrade performance. However, the seed for the MRTI remains an open question.

Another important consideration in current-driven metals is when and how plasma initiates on the Joule-heated surface [27,28]. Plasma formation on the liner outer surface can shunt current away from the liner [3,29] and develop magnetohydrodynamic (MHD) instabilities, reducing performance. The deleterious effects of plasma formation have inspired detailed one-dimensional (1D) MHD simulation studies of thermal plasma initiation [30,31]. However, experiments [32–35] show the process is three dimensional (3D), suggesting that to fully understand plasma formation and its later-time evolution, we must also consider its 3D nature, which we explore here.

A candidate for seeding both the MRTI and plasma formation is the electrothermal instability (ETI)

[23,36–41], driven by nonuniform Joule heating. In metals, where electrical conductivity σ falls with increasing temperature T (i.e., $d\sigma/dT < 0$), ETI predicts the formation of horizontal, overheated striations, oriented so as to rapidly grow through the MRTI. Once heated metal transforms into vapor, where $d\sigma/dT > 0$, ETI predicts the formation of overheated, vertical plasma filaments, in agreement with experiments. However, a basic question remains unanswered: how, exactly, do striations and filaments form? Given the orthogonal orientation of these modes, we anticipate this is a 3D process, requiring 3D seed perturbations. Metals commonly contain many such defects, including micrometer-scale resistive inclusions [32,42] and voids [43].

Defects force \mathbf{j} to deflect around and locally amplify, so that despite their small size, defects in general constitute *nonlinear* perturbations. For instance, the analogy between hydrodynamic and electrical current flow [44,45] shows that, independent of size, a spherical pit amplifies \mathbf{j} by a factor of 3/2 around the equator. This nonlinear perturbation $\delta\mathbf{j}$ initiates a feedback loop: the resulting enhanced Joule heating j^2/σ raises T , which lowers σ , further altering \mathbf{j} .

In this Letter, we use MHD simulations to show for the first time how a 3D nonlinear perturbation [i.e., a hemispherical pit on the metal surface, see Figs. 1(b) and 1(c)] self-consistently seeds both the striation and filament forms of ETI, through the feedback loop connecting \mathbf{j} and σ . The striation [Fig. 1(d)] is a hot strip aligned transverse to \mathbf{j} , which owing to its lower density ρ [Fig. 6(b)], serves as a seed to later MRTI growth. The filament [Fig. 1(e)] forms

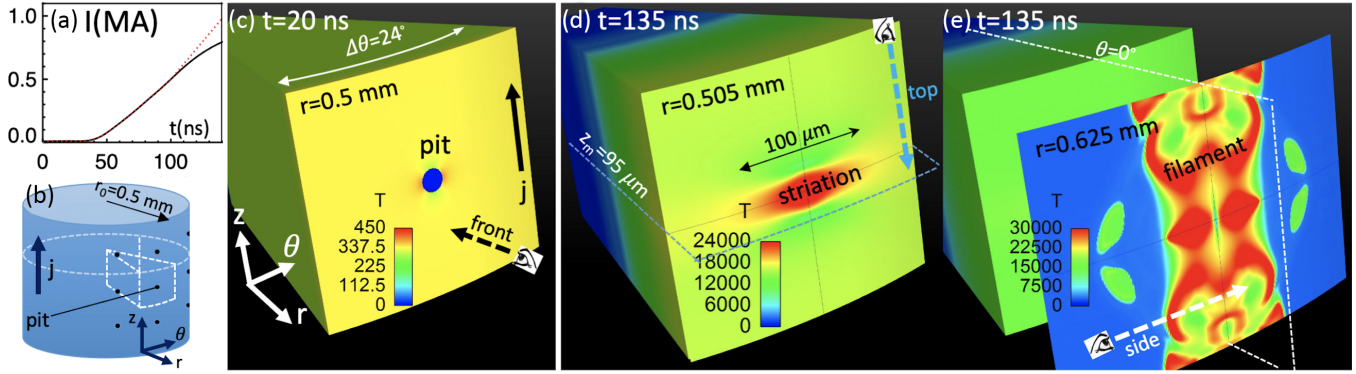


FIG. 1. (a) Current drive (black line) applied to (b) aluminum rod, with evenly spaced hemispherical pits on the outer face (only nine are shown). (c) Periodic wedge simulation demonstrates that a 20- μm -diameter pit seeds the formation of the (d) striation and (e) filament forms of ETI. Panels (c)–(e) show temperature $T(K)$, as well as viewing orientations. The top and side view visualize the axial midplane z_m and cross-sectional $\theta = 0^\circ$ plane, respectively.

later than the striation, but eventually coexists simultaneously with the striation, at larger radius in the lower- ρ vapor. The filament illustrates the 3D nature of plasma formation, achieving plasmalike temperatures earlier than an equivalent 1D simulation, owing to ETI-enhanced Joule heating. Finally, simulations predict that nonuniform heating seeded by the pit results in distinctive self-emission patterns, thus providing a means for experimental validation, recently accomplished in Ref. [46]. This experimental companion paper also briefly describes simulation results, to the extent necessary to understand the origins of the emission patterns, but does not address striation development or details of filament formation; we reserve this discussion for the present manuscript.

3D MHD simulation.—We use the MHD code ALEGRA [47] to model experiments [46] applying a current pulse $I(t)$ to a 1-mm-diameter aluminum rod, on the surface of which we machine hemispherical pits with radius $R = 10 \mu\text{m}$ (Fig. 1). Such rods achieve magnetic fields $B \sim 320 \text{ T}$, larger than the threshold at which aluminum forms thermally driven plasma [27], while also relevant to fields experienced by imploding liners discussed in the Introduction.

A SESAME equation of state [48] including material strength models the rod, which is initialized at room temperature $T_i = 294 \text{ K}$ (all units are SI). Electrical and thermal conductivities are provided by the Lee-More-Desjarlais model [49]. Simulations assume ion and electron temperatures are equal and do not account for radiative losses. To keep computations tractable, we only model a section of the rod using the wedge geometry shown in Figs. 1(b) and 1(c), with periodic boundary conditions in both the axial (z) and azimuthal (θ) directions. Further simulation details may be found in the companion paper [50].

Initial overheating and feedback due to pit.—Figures 2(a)–2(c) visualize the rod surface at early time, when the rod is

still solid. As described in Refs. [44,45], the flow of \mathbf{j} around obstacles can be understood in terms of its analogous ideal hydrodynamic flow. Hence, just as in hydrodynamic flow around an impenetrable sphere, the pit drives a flow pattern $\mathbf{j}_{\text{sphere}}$ in which \mathbf{j} deflects around the pit [see \mathbf{j} streamlines in Fig. 2(a)]. This deflection amplifies j around the equator, which in turn leads to enhanced j^2/σ there [Figs. 2(b) and 2(c)].

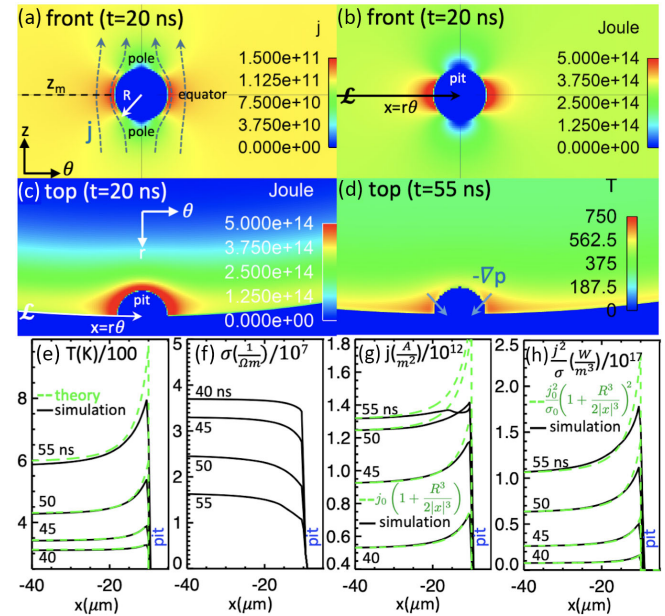


FIG. 2. Flow around a hemispherical pit, $\mathbf{j}_{\text{sphere}}$. Panels (a) and (b) visualize $j(\text{A}/\text{m}^2)$ and $j^2/\sigma(\text{W}/\text{m}^3)$ on the rod surface ($r = 0.5 \text{ mm}$). Representative \mathbf{j} streamlines (in blue) divert around the pit and amplify at the equator. (c) Top view visualizes enhanced j^2/σ around the pit. (d) T at a later time, showing focusing pressure gradient $-\nabla p$. (e)–(h) Azimuthal lineouts taken along \mathcal{L} , shown in (b) and (c). The edge of the pit lies at $x = -10 \mu\text{m}$. Legends use exponential notation, so $1\text{e}11$ corresponds to 1×10^{11} .

When σ is spatially constant (i.e., $\sigma = \sigma_0$), \mathbf{j} and j^2/σ can be expressed simply along the azimuthal lineout \mathcal{L} shown in Figs. 2(b) and 2(c):

$$\mathbf{j}_{\text{sphere}}(|x| \geq R) = j_0(t) \left(1 + \frac{R^3}{2|x|^3} \right) \hat{z}, \quad (1)$$

$$\frac{j_{\text{sphere}}^2}{\sigma}(|x| \geq R) = \frac{j_0(t)^2}{\sigma_0(t)} \left(1 + \frac{R^3}{2|x|^3} \right)^2, \quad (2)$$

where $x = r\theta$ is the distance from pit center and $j_0(t)$ is the unperturbed value of j , far from the pit. Figures 2(e)–2(h) plot the $x < 0$ portion of $T, \sigma, j, j^2/\sigma$ along \mathcal{L} at several times (profiles are symmetric about $x = 0$). At $t = 40$ ns, σ is approximately constant and Eqs. (1) and (2) match simulation.

The pit edge $x \sim -R$ experiences the highest $j^2/\sigma, T$ increase, and σ decrease, initiating the aforementioned feedback loop connecting \mathbf{j} and σ . By $t = 50$ ns, $\sigma(x \sim -R)$ has decreased sufficiently compared to its unperturbed value $\sigma_0 \equiv \sigma(x \gg R)$ that j deviates significantly from Eq. (1). Nevertheless, Fig. 2(h) shows the j^2/σ profile remains relatively insensitive to variations in σ —the electric field E in lower- σ regions rises, partially compensating for reduced σ in $j^2/\sigma = \sigma E^2$. Consequently, we can solve for the T profile:

$$T(|x| > R, t) \simeq T_i + \left(1 + \frac{R^3}{2|x|^3} \right)^2 \frac{\eta_i}{2} \frac{dj}{dt} (e^{\int_0^t \gamma_0 dt} - 1), \quad (3)$$

with growth rate $\gamma_0 = [(d\eta/dT)j_0(t)^2/\rho c_V]$, where $\eta(T) \equiv 1/\sigma(T)$ is the electrical resistivity, $\eta_i \equiv \eta(T = T_i)$, $(d\eta/dT)$ is assumed constant, and c_V is the specific heat. Further details on the derivation of Eq. (3) may be found in Supplemental Material [51]. Equation (3) approximately matches simulation up through $t = 50$ ns, and can thus predict nonlinear δT perturbations. However, by $t = 55$ ns, $\delta\sigma$ is sufficiently large that the fit (2) starts to fail, so Eq. (3) overpredicts $T(x \sim -R)$.

Striation development.—In solid metal, the MHD equation of motion $\rho(d\mathbf{v}/dt) = -\nabla p + \mathbf{j} \times \mathbf{B}$ generalizes to $\rho(d\mathbf{v}/dt) = \nabla \cdot \mathbf{T} + \mathbf{j} \times \mathbf{B}$, where the stress tensor $T_{ij} \equiv -\delta_{ij}p + T'_{ij}$ includes both thermal pressure p and deviatoric stress T'_{ij} , which accounts for material strength of the solid. At $t = 55$ ns, the $\mathbf{j} \times \mathbf{B}$ force and tensile deviatoric stress, which point radially inward, approximately balance the outward-pointing pressure gradient $-\nabla p$ at the rod surface. However, after the surface melts, material strength vanishes and the melt-induced decrease in σ causes j and $\mathbf{j} \times \mathbf{B}$ to fall. Consequently $-\nabla p$ dominates and initiates hydrodynamic expansion, altering the σ “topography.”

The overheated region around the pit is hottest and expands first. As shown in Fig. 2(d), the void creates a $-\nabla p$ which azimuthally *focuses* the resulting expansion, similar to the “shaped-charge” effect [57,58]. This concentration of metal into the pit center forms a bump (Fig. 3), while also

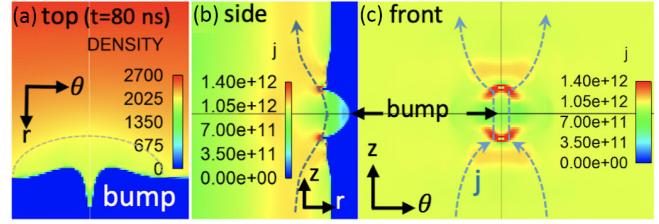


FIG. 3. (a) Top view of density ρ (kg/m^3), showing how overheated metal around the pit’s equator has expanded, forming a bump which qualitatively changes the \mathbf{j} flow pattern. (b) Side view, showing j peaking at the base of the bump. (c) Front view of j near rod surface ($r = 0.499$ mm). All panels show $t = 80$ ns.

resulting in a lower- ρ region behind the bump [bounded by the gray curve in Fig. 3(a)]. Consequently, \mathbf{j} no longer deflects *around* a pit (i.e., azimuthally away and radially inward), but rather flows *into* the bump (i.e., azimuthally toward and radially outward), as illustrated by \mathbf{j} streamlines in Figs. 3(b) and 3(c). In the 2D (r, z) solution for hydrodynamic flow over a bump [50,59], flow is fastest at the base of the bump, where the surface transitions from curved to flat. Similarly, in our electrical problem, \mathbf{j} peaks at the bump base [Figs. 3(b) and 3(c)], leading to peaks in j^2/σ there. This flow pattern contrasts with the original $\mathbf{j}_{\text{sphere}}$ solution [Fig. 2(a)].

Later, the “bump flow”-driven Joule heating pattern persists at the rod surface [Fig. 4(a)] and drives hot spots

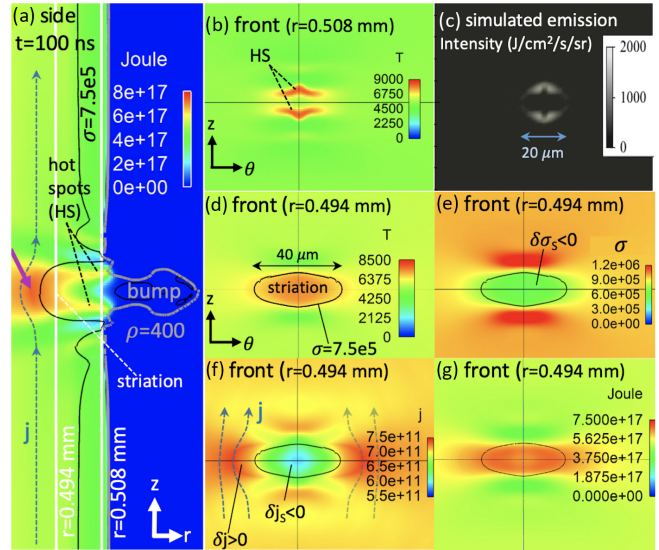


FIG. 4. (a) The Joule heating pattern arising from bump flow drives hot spots (HS) near the rod surface (visualized by $\rho_{\text{crit}} = 400$ (kg/m^3) contour), as well as a striation deeper in the metal. The HS, visualized in (b), are observable in (c) visible self-emission. The striation in (d)–(g) has lower electrical conductivity $\sigma(1/\Omega\text{m})$ relative to surrounding metal, forcing \mathbf{j} to divert around and amplify at the edges. The resulting enhanced Joule heating drives striation growth azimuthally and radially. All panels show $t = 100$ ns.

(HS), visualized in Fig. 4(b). Simulated visible self-emission [Fig. 4(c)], generated using the postprocessing code SPECT3D [60], shows the HS and allows comparison to experiment [46], which have indeed validated this prediction. Figure 4(c) does not resolve another overheated structure that lies too deep within the metal to be visible in self-emission. This structure—a nascent ETI striation—is visualized in Fig. 4(d). The striation, roughly bounded by the $\sigma = 7.5 \times 10^5$ ($1/\Omega\text{m}$) contour, is broader than the HS in Fig. 4(b), as well as lower ρ than surrounding metal. Its origin traces back to the overheated metal surrounding the pit in Fig. 2, which expands, resulting in the hotter, lower- ρ region bounded by the gray curve in Fig. 3(a). Since $d\sigma/d\rho > 0$ in the solid and liquid phases (e.g., Fig. 1 in Ref. [50]), lower ρ and higher T in the striation results in lower σ there [i.e., using a subscripted S to denote the striation, $\delta\sigma_S < 0$ in Fig. 4(e)], and consequently lower j [$\delta j_S < 0$ in Fig. 4(f)]. Nevertheless, the striation continues to overheat through enhanced j^2/σ [Fig. 4(g)], because the increase in j^2/σ due to $\delta\sigma_S < 0$ overcomes the reduction due to $\delta j_S < 0$.

The $\delta\sigma_S < 0$ causes \mathbf{j} to divert azimuthally around the striation, as sketched in Fig. 4(f), so j and j^2/σ amplify at the edges, similar to flow around the pit. In this way, the striation continuously widens by converting high- σ , dense metal at the edges into hotter, expanded, lower- σ metal, characteristic of the striation. The \mathbf{j} redistribution responsible for striation widening also applies radially: as seen in Fig. 4(a), the striation constitutes a low- σ divot which forces \mathbf{j} to divert inward and amplify at the divot tip [50,59]. Consequently, a local peak in j^2/σ develops there [magenta arrow in Fig. 4(a)], and the resulting overheating allows the striation to propagate radially. These current redistribution processes, also described in Ref. [39], allow the pit to seed structures in the metal that are several times the original pit size.

Filament and crater formation.—Eventually, the overheated HS in Figs. 4(a) and 4(b) explode, creating expanding plumes and craters [Fig. 5(a)]. The black $\rho_{\text{crit}} = 400$ (kg/m^3) contour is close to the critical density ~ 375 (kg/m^3) [48], and thus roughly visualizes the boundary between liquid metal and dense vapor.

In Figs. 5(b)–5(e), the HS have expanded into the vapor phase, where $d\sigma/dT > 0$ (opposite to solids and liquids). Consequently, in contrast to Fig. 4(e), where the hotter striation represented a minimum in σ (relative to surrounding metal), now the HS correspond to peaks in σ . Hence, the HS can satisfy the feedback loop required for the filament form of ETI: $\delta T_{\text{HS}} > 0 \Rightarrow \delta\sigma_{\text{HS}} > 0 \Rightarrow \delta j_{\text{HS}} > 0 \Rightarrow \delta(j^2/\sigma)_{\text{HS}} > 0 \Rightarrow dT_{\text{HS}} > 0$. Just as in striation formation, \mathbf{j} redistribution plays a vital role in HS-filament formation, now *concentrating* in the HS and providing enhanced j^2/σ to compete with pdV cooling (i.e., work done in changing volume from V to $V + dV$) during plume expansion.

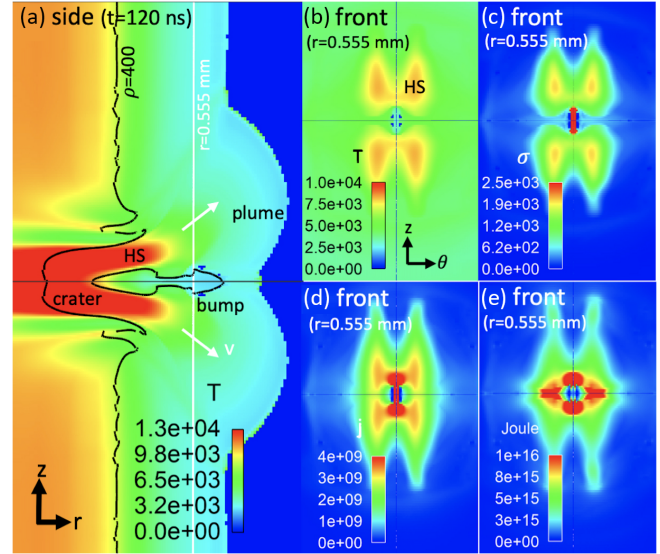


FIG. 5. (a) The HS explode, resulting in plumes as well as craters on the rod surface (visualized by the $\rho = 400$ kg/m^3 contour). (b)–(e) In the vapor phase, $d\sigma/dT > 0$ (i.e., opposite to solid-liquid phase), so the HS have enhanced σ . This initiates the ETI feedback loop driving filament formation. All panels show $t = 120$ ns.

As the HS explode, they expand axially, as sketched by the velocity vectors \mathbf{v} in Fig. 5(a). However, in the azimuthal direction, \mathbf{v} initially *focuses* before later expanding. As described in Ref. [50], this focusing is due to the shaped-charge effect, also responsible for converting the pit into a bump in Fig. 3. Because of this hydrodynamic flow asymmetry, the HS grow faster axially than azimuthally, leading to the axially elongated filament [Figs. 5(b)–5(e)] predicted by ETI.

By $t = 135$ ns, the filament spans the computational domain and ETI-enhanced j^2/σ achieves plasmalike temperatures in the filament [compare Figs. 1(e) and 5(b)], which dominates self-emission in Fig. 6(a). An equivalent 1D simulation, which models a perfectly smooth rod using the same radial resolution as 3D, also demonstrates plasma formation. However, because 1D cannot resolve j concentration in the filament and the resulting enhanced j^2/σ , the 1D simulation forms plasma ~ 17 ns later than 3D, as discussed in Ref. [50].

Inside the metal, the striation has continued to overheat and widen [compare Figs. 1(d) and 4(d)], through the \mathbf{j} redistribution process described earlier. Because of the expulsion of overheated material through the plumes, the hot band seen in Fig. 1(d) also corresponds to a region of lower ρ [Fig. 6(b)]. For instance, ρ at the center of the striation (identified by ρ_S) is $2.6\times$ lower than the unperturbed value ρ_0 . Hence, the pit has seeded a crater that is roughly $4\times$ deeper [Fig. 6(c)] and $5\times$ wider than the original pit size, providing a seed for the MRTI, which is triggered when the rod surface starts to accelerate radially inward.

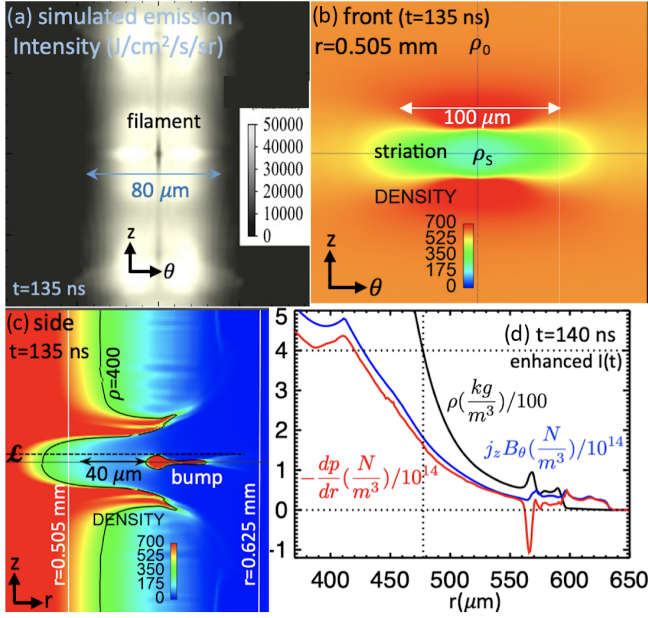


FIG. 6. (a) The filament resides in the low- ρ vapor at $r \sim 0.625$ mm—see (c)—and dominates visible self-emission. (b),(c) The pit has seeded a ρ perturbation approximately $5\times$ wider and $4\times$ deeper than the original size. In (d), radial lineouts along \mathcal{L} show the inward-pointing $j_z B_\theta$ force overcomes the outward-pointing pressure gradient $-dp/dr$, so the ρ_{crit} contour is MRT unstable. All panels show $t = 135$ ns, although (d) considers a separate simulation at $t = 140$ ns, driven with enhanced $I(t)$ shown in red in Fig. 1(a).

In this case, in the accelerated frame moving with the rod surface, the effective gravity points radially outward, so that lighter fluid supports heavier fluid (the usual scenario in the Rayleigh-Taylor instability). Taking the radial component of the equation of motion yields $\rho(dv_r/dt) \simeq -(dp/dr) - j_z B_\theta$. Hence, in order to achieve inward acceleration $(dv_r/dt) < 0$, the inward-pointing $j_z B_\theta$ term must overcome the outward-pointing pressure gradient $-(dp/dr)$.

In the simulation considered here, this condition is satisfied locally in the filament (due to enhanced j), but not over the bulk of the rod surface. In particular, the maximum current $I_{\text{max}} \sim 0.85$ MA is insufficient to achieve $j_z B_\theta > -(dp/dr)$ at the ρ_{crit} crater surface, which will consequently not seed the MRTI. However, consider a simulation driven with larger current [see red curve in Fig. 1(a)], which at $t = 140$ ns reaches $I \sim 1$ MA and exhibits $\rho(\mathbf{r})$ similar to Fig. 6(c). For the enhanced- I case, Fig. 6(d) plots $j_z B_\theta$ and $-(dp/dr)$ along radial lineout \mathcal{L} (which lies slightly above the axial midplane to avoid complications from the bump remnant). Over the range observed, $j_z B_\theta \geq -(dp/dr)$, so the crater at ρ_{crit} serves as a seed for the MRTI.

Summary.—MHD simulations reveal the impact of commonly occurring defects in current-driven metal: feedback between \mathbf{j} and σ allows a defect to self-consistently

seed both the larger striation and filament structures predicted by ETI. The striation constitutes a wider, deeper density perturbation that seeds the MRTI, as illustrated in Fig. 6; the filament provides an accelerated path to plasma formation, through 3D \mathbf{j} redistribution. Recent experiments [46] using ultrapure aluminum rods with machined pits have verified the self-emission predictions in Figs. 4(c) and 6(a), thus providing credibility to the simulations. Although the scope of this study is narrow, we have started testing the robustness of results by varying simulation parameters (e.g., dielectric-filled pits, differently shaped pits, higher (dI/dt) , MagLIF-like liners [12–17] driven by 20 MA current) and found qualitatively similar behavior. This result suggests the physical processes described here have a universal character, and constitute building blocks toward a 3D theory of defect evolution in current-driven metal.

We hope the present Letter will lead to improved computational predictive capability for targets driven by intense current, used in a wide array of applications. While metal is commonly modeled as a homogeneous medium, accounting for defects should result in more accurate metal evolution and plasma formation. Although it is not currently feasible to model an entire target and its associated 3D defects (due to resolution limitations), understanding the interaction of a smaller collection of defects could lead to better-informed initial conditions for larger, lower-resolution design calculations. Furthermore, studies of defect interaction may elucidate mysteries in the development of 3D structures in imploding liners, such as a helixlike instability in liners premagnetized with an axial magnetic field [61]. Finally, practically speaking, this Letter highlights the importance of material and surface characterization.

E. P. Y. thanks M. Cuneo and A. Velikovich for valuable input in preparing this manuscript, K. Beckwith for programmatic support, and the anonymous referees for elevating the scientific content through their challenging questions. We benefited from stimulating discussion with D. Yager-Elorriaga, G. Shipley, E. Harding, S. Kreher, A. Klemmer, J. Chittenden, F. Doss, N. Fisch, L. Elgin, R. Vesey, K. Blaha, M. Weis, T. Mehlhorn, M. Desjarlais, M. Gilmore, D. Ruiz, W. Tatum, Y. Maron, S. Hansen, B. Jones, N. Bennett, E. Evstatiev, and M. Gomez. We thank A. C. Robinson, J. Niederhaus, and C. Siefert for Alegra guidance and I. Golovkin for help with SPECT3D. This research was supported by the Sandia Laboratory Directed Research and Development Program under Projects No. 178661 and No. 200269. Part of this work was performed under the auspices of the U.S. Department of Energy by Lawrence Livermore National Laboratory under Contract No. DE-AC52-07NA27344. Sandia National Laboratories is a multimission laboratory managed and operated by National Technology and Engineering Solutions of Sandia LLC, a wholly owned subsidiary of Honeywell International Inc. for the

U.S. Department of Energy's National Nuclear Security Administration under Contract No. DE-NA0003525. This Letter describes objective technical results and analysis. Any subjective views or opinions that might be expressed in the Letter do not necessarily represent the views of the U.S. Department of Energy or the United States Government.

*epyu@sandia.gov

- [1] D. Sinars, M. A. Sweeney, C. S. Alexander, D. J. Ampleford, T. Ao *et al.*, *Phys. Plasmas* **27**, 070501 (2020).
- [2] R. W. Lemke, M. D. Knudson, D. E. Bliss, K. R. Cochrane, J.-P. Davis, A. A. Giunta, H. C. Harjes, and S. A. Slutz, *J. Appl. Phys.* **98**, 073530 (2005).
- [3] P. A. Gourdain, M. B. Adams, M. Evans, H. R. Hasson, R. V. Shapovalov, J. R. Young, and I. West-Abdallah, *Phys. Plasmas* **26**, 042706 (2019).
- [4] S. N. Bland, Ya. E. Krasik, D. Yanuka, R. Gardner, J. MacDonald, A. Virozub, S. Efimov, S. Gleizer, and N. Chaturvedi, *Phys. Plasmas* **24**, 082702 (2017).
- [5] M. D. Knudson, M. P. Desjarlais, A. Becker, R. W. Lemke, K. R. Cochrane, M. E. Savage, D. E. Bliss, T. R. Mattsson, and R. Redmer, *Science* **348**, 1455 (2015).
- [6] B. Jones, C. A. Coverdale, C. Deeney, D. B. Sinars, E. M. Waisman, M. E. Cuneo, D. J. Ampleford, P. D. Lepell, K. R. Cochrane, J. W. Thornhill *et al.*, *Phys. Plasmas* **15**, 122703 (2008).
- [7] D. J. Ampleford, C. A. Jennings, B. Jones, S. B. Hansen, M. E. Cuneo, C. A. Coverdale, M. C. Jones, T. M. Flanagan, M. Savage, W. A. Stygar, M. R. Lopez, J. P. Apruzese, J. W. Thornhill, J. L. Giuliani, and Y. Maron, *Phys. Plasmas* **20**, 103116 (2013).
- [8] S. V. Lebedev, A. Frank, and D. D. Ryutov, *Rev. Mod. Phys.* **91**, 025002 (2019).
- [9] J. E. Bailey, T. Nagayama, G. P. Loisel, G. A. Rochau, C. Blancard, J. Colgan, Ph. Cosse, G. Faussurier, C. J. Fontes, F. Gilleron *et al.*, *Nature (London)* **517**, 56 (2015).
- [10] H. Knoepfel, *Pulsed High Magnetic Fields* (North-Holland Publishing Company, Amsterdam, 1970).
- [11] G. A. Shneerson, M. I. Dolotenko, and S. I. Krivosheev, *Strong and Superstrong Pulsed Magnetic Fields Generation* (de Gruyter, Berlin, 2014).
- [12] S. A. Slutz, M. C. Herrmann, R. A. Vesey, A. B. Sefkow, D. B. Sinars, D. C. Rovang, K. J. Peterson, and M. E. Cuneo, *Phys. Plasmas* **17**, 056303 (2010).
- [13] M. R. Gomez, S. A. Slutz, A. B. Sefkow, D. B. Sinars, K. D. Hahn, S. B. Hansen, E. C. Harding, P. F. Knapp, P. F. Schmit, C. A. Jennings *et al.*, *Phys. Rev. Lett.* **113**, 155003 (2014).
- [14] M. E. Cuneo *et al.*, *IEEE Trans. Plasma Sci.* **40**, 3222 (2012).
- [15] M. R. Gomez, S. A. Slutz, C. A. Jennings, D. J. Ampleford, M. R. Weis *et al.*, *Phys. Rev. Lett.* **125**, 155002 (2020).
- [16] A. B. Sefkow, S. A. Slutz, J. M. Koning, M. M. Marinak, K. J. Peterson, D. B. Sinars, and R. A. Vesey, *Phys. Plasmas* **21**, 072711 (2014).
- [17] D. A. Yager-Elorriaga *et al.*, *Nucl. Fusion* **62**, 042015 (2022).
- [18] M. M. Basko, A. J. Kemp, and J. Meyer-ter-Vehn, *Nucl. Fusion* **40**, 59 (2000).
- [19] I. R. Lindemuth, *Phys. Plasmas* **22**, 122712 (2015).
- [20] V. Mokhov, O. Burenkov, A. Buyko, S. Garanin, S. Kuznetsov, V. Mamyshev, A. Startsev, and V. Yakubov, *Fusion Eng. Des.* **70**, 35 (2004).
- [21] P. F. Schmit and D. E. Ruiz, *Phys. Plasmas* **27**, 062707 (2020).
- [22] E. G. Harris, *Phys. Fluids* **5**, 1057 (1962).
- [23] D. D. Ryutov, M. S. Derzon, and M. K. Matzen, *Rev. Mod. Phys.* **72**, 167 (2000).
- [24] Y. Zhou, R. J. R. Williams, P. Ramaprabhu, M. Groom, B. Thornber, A. Hillier, W. Mostert, B. Rollin, S. Balachandrar, P. D. Powell, A. Mahalov, and N. Attal, *Physica (Amsterdam)* **423D**, 132838 (2021).
- [25] D. E. Ruiz, D. A. Yager-Elorriaga, K. J. Peterson, D. B. Sinars, M. R. Weis, D. G. Schroen, K. Tomlinson, J. R. Fein, and K. Beckwith, *Phys. Rev. Lett.* **128**, 255001 (2022).
- [26] R. D. McBride, S. A. Slutz, C. A. Jennings, D. B. Sinars, M. E. Cuneo, M. C. Herrmann, R. W. Lemke, M. R. Martin, R. A. Vesey, K. J. Peterson *et al.*, *Phys. Rev. Lett.* **109**, 135004 (2012).
- [27] T. J. Awe, B. S. Bauer, S. Fuelling, and R. E. Siemon, *Phys. Rev. Lett.* **104**, 035001 (2010).
- [28] D. Zhang, J. Wu, Z. Chen, Y. Lu, H. Shi, G. Wang, D. Xiao, N. Ding, X. Li, S. Jia, and A. Qiu, *Phys. Plasmas* **27**, 062709 (2020).
- [29] D. Mikitchuk, M. Cvejić, R. Doron, E. Kroupp, C. Stollberg, Y. Maron, A. L. Velikovich, N. D. Ouart, J. L. Giuliani, T. A. Mehlhorn, E. P. Yu, and A. Fruchtman, *Phys. Rev. Lett.* **122**, 045001 (2019).
- [30] S. F. Garanin, S. D. Kuznetsov, W. L. Atchison, R. E. Reinovsky, T. J. Awe, B. S. Bauer, S. Fuelling, I. R. Lindemuth, and R. E. Siemon, *IEEE Trans. Plasma Sci.* **38**, 1815 (2010).
- [31] I. R. Lindemuth, R. E. Siemon, B. S. Bauer, M. A. Angelova, and W. L. Atchison, *Phys. Rev. Lett.* **105**, 195004 (2010).
- [32] T. J. Awe, E. P. Yu, K. C. Yates, W. G. Yelton, B. S. Bauer, T. M. Hutchinson, S. Fuelling, and B. B. McKenzie, *IEEE Trans. Plasma Sci.* **45**, 584 (2017).
- [33] A. M. Steiner, P. C. Campbell, D. A. Yager-Elorriaga, N. M. Jordan, R. D. McBride, Y. Y. Lau, and R. M. Gilgenbach, *IEEE Trans. Plasma Sci.* **46**, 3753 (2018).
- [34] K. C. Yates, T. J. Awe, B. S. Bauer, T. M. Hutchinson, E. P. Yu, S. Fuelling, D. C. Lampa, and M. R. Weis, *Phys. Plasmas* **27**, 082707 (2020).
- [35] S. C. Bott-Suzuki, S. W. Cordaro, L. Atoyán, T. Byvank, W. Potter, B. R. Kusse, J. B. Greenly, D. A. Hammer, and C. A. Jennings, *IEEE Trans. Plasma Sci.* **46**, 1921 (2018).
- [36] M. G. Haines, *J. Plasma Phys.* **12**, 1 (1974).
- [37] V. I. Oreshkin, *Phys. Plasmas* **15**, 092103 (2008).
- [38] K. J. Peterson, D. B. Sinars, E. P. Yu, M. C. Herrmann, M. E. Cuneo, S. A. Slutz, I. C. Smith, B. W. Atherton, M. D. Knudson, and C. Nakhleh, *Phys. Plasmas* **19**, 092701 (2012).
- [39] J. D. Pecover and J. P. Chittenden, *Phys. Plasmas* **22**, 102701 (2015).

- [40] T. M. Hutchinson, T. J. Awe, B. S. Bauer, K. C. Yates, E. P. Yu, W. G. Yelton, and S. Fuelling, *Phys. Rev. E* **97**, 053208 (2018).
- [41] V. I. Oreshkin, R. B. Baksht, E. V. Oreshkin, A. G. Rousskikh, and A. S. Zhigalin, *Plasma Phys. Controlled Fusion* **62**, 035016 (2020).
- [42] S. Kuyucak and R. I. L. Guthrie, *Can. Metall. Q.* **28**, 41 (1989).
- [43] T. Sakurai, Y. Kohmura, A. Takeuchi, Y. Suzuki, S. Goto, and T. Ishikawa, *AIP Conf. Proc.* **879**, 1380 (2007).
- [44] H. Lamb, *Hydrodynamics*, 6th ed. (Dover, New York, 1932), p. 65.
- [45] E. P. Yu, T. J. Awe, K. R. Cochrane, K. C. Yates, T. M. Hutchinson, K. J. Peterson, and B. S. Bauer, *Phys. Plasmas* **27**, 052703 (2020).
- [46] T. J. Awe, E. P. Yu, M. W. Hatch, T. M. Hutchinson, K. Tomlinson, W. D. Tatum, K. C. Yates, B. T. Hutzel, and B. S. Bauer, *Phys. Plasmas* **28**, 072104 (2021).
- [47] A. C. Robinson and C. J. Garasi, *Comput. Phys. Commun.* **164**, 408 (2004).
- [48] T. Sjostrom, S. Crockett, and S. Rudin, *Phys. Rev. B* **94**, 144101 (2016).
- [49] M. P. Desjarlais, J. D. Kress, and L. A. Collins, *Phys. Rev. E* **66**, 025401 (2002).
- [50] E. P. Yu, T. J. Awe, K. R. Cochrane, K. J. Peterson, K. C. Yates, T. M. Hutchinson, M. W. Hatch, B. S. Bauer, K. Tomlinson, and D. B. Sinars, companion paper, *Phys. Rev. E* **107**, 065209 (2023).
- [51] See Supplemental Material at <http://link.aps.org/supplemental/10.1103/PhysRevLett.130.255101> for derivation of early time, ETI-driven temperature perturbation due to a 3D, nonlinear perturbation, which includes Refs. [52–56].
- [52] V. I. Oreshkin and S. A. Chaikovsky, *Phys. Plasmas* **19**, 022706 (2012).
- [53] A. L. Velikovich, A. J. Schmitt, C. Zulick, Y. Aglitskiy, M. Karasik, S. P. Obenschain, J. G. Wouchuk, and F. Cobos Campos, *Phys. Plasmas* **27**, 102706 (2020).
- [54] S. M. Ponomarev, *U.S.S.R. Comput. Maths. Math. Phys.* **28**, 177 (1988).
- [55] Ya. B. Zel'dovich and Yu. P. Raizer, *Physics of Shock Waves and High-Temperature Hydrodynamic Phenomena* (Dover Publications, New York, 2002).
- [56] H. A. Haus and J. R. Melcher, *Electromagnetic Fields and Energy* (Prentice-Hall, Englewood Cliffs, New Jersey, 1989).
- [57] C. E. Munroe, *Am. J. Sci.* **36**, 48 (1888).
- [58] W. Walters, *Fundamentals of Shaped Charges* (CMC Press, Baltimore, MD, 1998).
- [59] L. M. Milne-Thomson, *Theoretical Hydrodynamics* (Dover, New York, 1968), p. 177.
- [60] J. J. MacFarlane, I. E. Golovkin, P. Wang, P. R. Woodruff, and N. A. Pereyra, *High Energy Density Phys.* **3**, 181 (2007).
- [61] T. J. Awe, R. D. McBride, C. A. Jennings, D. C. Lamppa, M. R. Martin *et al.*, *Phys. Rev. Lett.* **111**, 235005 (2013).